Supporting Information

Single-Molecule-Level Detection of Interfacial Molecular Structures and Ultrafast Dynamics

Xiaoxuan Zheng[1,2], Junjun Tan[2,], Quanbing Pei[1], Yi Luo[1,2,*], Shuji Ye[1,2,*]*

[1]Hefei National Research Center for Physical Sciences at the Microscale, Department of Chemical Physics, University of Science and Technology of China, Hefei, Anhui, 230026, China

[2]Hefei National Laboratory, University of Science and Technology of China, Hefei, Anhui 230088, China

*To whom all correspondence should be addressed.

Email: shujiye@ustc.edu.cn

Tel: 086-551-3603462

Table of contents

1. Experimental section

1.1 Materials and sample preparation

4-Nitrothiophenol (NTP, with a purity >95%) was obtained from Aladdin. 4-Mercaptobenzonitrile (MBN, with a purity >97%) was obtained from Shanghai Haohong Scientific Co., Ltd. Ethanol and n-hexane were purchased from Sinopharm Chemical Reagent Co., Ltd. Ultrapure deionized (DI) water was purified by a Milli-Q reference system. All the chemicals were used as received.

The samples were prepared by the following method: first, a clean smooth gold film (a 10 nm thick Cr layer was evaporated onto a rotating silicon wafer, followed by a 100 nm thick Au layer) was soaked in the target molecular solution (in ethanol) at room temperature (24 ℃) overnight to obtain a well-assembled self-assembled monolayer (SAM). The mixed SAMs were prepared using 10 mM solutions of NTP and MBN in molar ratios varying from 10:0 (100% NTP) to 0:10 (0% NTP). In the dilution experiments, all solutions were contained in 30 mL washed and dried brown glass bottles. The experimental procedure was conducted as follows: first, NTP solid powder was accurately weighed to prepare an initial solution of 10^{-2} M, which was then subjected to ultrasonication to ensure complete and uniform dispersion. Subsequently, a precise volume of the solution was transferred using a pipette into the glass bottles, followed by serial dilution with ethanol. After each dilution step, the solution was ultrasonicated to achieve homogeneity before proceeding to the next concentration gradient. Through this sequential dilution method, a series of solutions with

varying concentrations were obtained, with each concentration gradient precisely adjusted to a final volume of 10 mL. It is noteworthy that, to ensure the accuracy and reliability of the experimental results, all experiments were performed using brand-new glass containers that had undergone rigorous cleaning and drying processes. Additionally, fresh solutions were prepared and diluted for each experiment. A series of concentrations (*C*) of NTP SAMs were prepared by submerging gold films in 10 mL of a certain concentration of an ethanol solution of NTP. The sample was subsequently removed and washed with ethanol several times to eliminate physical adsorption. NPoMs were made by dispersing gold nanoparticles (Au NPs) on Au-SAM. Au NPs with a diameter of approximately 55 nm were synthesized.[1] Specifically speaking, 200 mL of 0.01 wt% $HAuCl_4$ solution was added to a three-neck round-bottom flask and then heated to boiling under vigorous stirring. Then, 1.4 mL of 1 wt% sodium citrate solution was quickly added to the boiling solution, after which the mixture was boiled and stirred for 1 hour. Finally, the AuNP solution was cooled to room temperature. The Au nanoparticles used in this study were citrate-stabilized rather than shell-isolated. Then, the target molecules were covered with a layer of closely packed AuNPs using the Langmuir-Blodgett (L-B) method,[2, 3] and a relatively uniform and dense NPoM structure was formed (named NPoM-SAMs). In L-B method, 10~15 mL of AuNP solution were placed in a cleaned glass dish, and 3~4 mL of n-hexane was added to the top of the colloid solution to form an immiscible hexane/water interface. Then enough ethanol was slowly injected into the surface of the hexane/water layers using a syringe, which

resulted in the AuNPs escaping from the colloid solution to the interface and becoming trapped at the interface. After the complete volatilization of n-hexane, the dispersed AuNPs were assembled into a close-packed 2D array, transferred onto a cleaned Au film, and dried at ambient temperature. It should be mentioned that this "L-B method" is different from the traditional L-B method in the measurement of a pressure-area isotherm diagram. The samples without AuNPs were named as Au-SAMs. The specific sample preparation schematic is shown in Figure S1. It should be emphasized that the *C* mentioned in this work refers to the concentration of the solution that was used to prepare the sample and it does not mean that the experiments were performed in that solution.

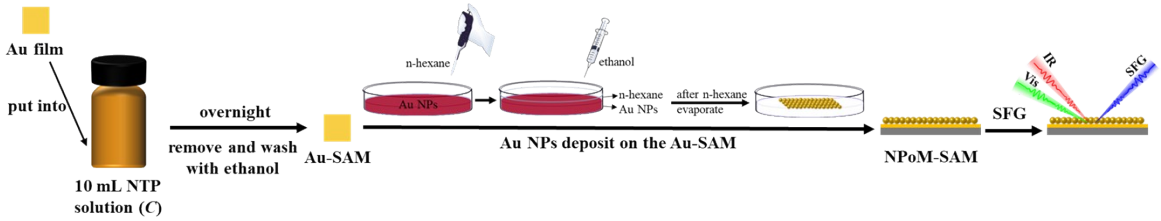

Figure S1. Preparation schematic of the samples (Au-SAM and NPoM-SAM) used for testing.

1.2 Sum-frequency generation (SFG) setups and experiments

In this work, we used two experimental SFG setups to carry out the SFG measurements. Setup 1 with a geometry in a noncollinear configuration was employed for collecting SFG vibrational spectra (Figure 1 and Figure S2). Setup 2 with a geometry in a collinear configuration was used to SFG imaging measurements (Figure S3).

a) Sum-frequency generation vibrational spectroscopy (SFG-VS) experiments

All SFG experiments were carried out using a femtosecond time-resolved SFG-VS system. Detailed information about the instrument parameters was provided in our previous studies.[4, 5] To avoid IR absorption by water vapor, we purged the light path chamber using dry air provided by the Orion air dryer (CRX 5J, Orion Machinery Co., Ltd, Dongguan, China) to maintain a relative humidity below 2%. All SFG experiments were carried out at room temperature (24°C). The SFG signals were generated by focusing the IR and visible beams on the sample surface with a focused spot diameter of ~ 200 μm. The incident angles for the IR and visible beams were 45° and 60°, respectively. The SFG spectra of interfacial molecules with ppp (p-polarized SFG output, p-polarized visible input, and p-polarized infrared input) were collected. In order to ensure the accuracy of the peak frequencies, we used a standard polystyrene film (ps film) for frequency correction. The SFG spectra were normalized by measuring the energy profile of the IR pulses determined by SFG signals from GaAs (110). To compare absolute SFG intensities, we normalized the exposure time as well. The SFG signals were detected by an EMCCD camera (Newton 970 BVF, Andor) and dispersed into a spectrometer (Samrock 303i, Andor). In our SFG system, the width of visible pulse is about 4 cm^{-1}. However, the frequency fluctuation of the visible pulse for different repeated measurements under the same conditions is better than 0.3 cm^{-1}. Such small fluctuations result in a spectral deviation of ~ 0.3 cm^{-1}.

For the SFG-FID instrumentation (Figure S2c),[6] it was required to remove the pulse

shaper device for the 800 nm visible light in the frequency domain spectral measurement system and to change the visible light into femtosecond light as well. In the FID experiments, the pulse duration of IR and vis beams is ~ 100 fs. In the broadband SFG measurements, the pulse duration of vis beam was stretched to ~ 6 ps. The area of the spectra obtained at each delay time is used as the signal intensity of the time-domain spectra, and the delay time corresponding to the highest point of the signal is set as the time zero point. In this experiment, the IR delay ranged from -1 ps to 4 ps with a time interval of 100 fs.

For the IR pump- SFG probe time-resolved SFG instrumentation (Figure S2d), the incident angle of the pump IR was 53°. The pulse energies of the pump IR and probe IR pulses were ~8 μJ and 8 μJ at ~1340 cm^{-1}, respectively. The pulse energy of Vis was 0.4 μJ. The pump IR was separated by an optical chopper to produce pump-on and pump-off SFG signals, which were split by a galvo mirror and imaged onto different rows of the CCD chip. A LABVIEW program was used to control the delay time between the pump IR pulse and the probe IR pulse. According to the ratio of the processed pump-on and pump-off spectra for the corresponding delay time, the population information of the ground state-excited state at a certain delay time is determined. The specific spectral fitting procedures and data analysis have been presented in our previous publications.[4, 7]

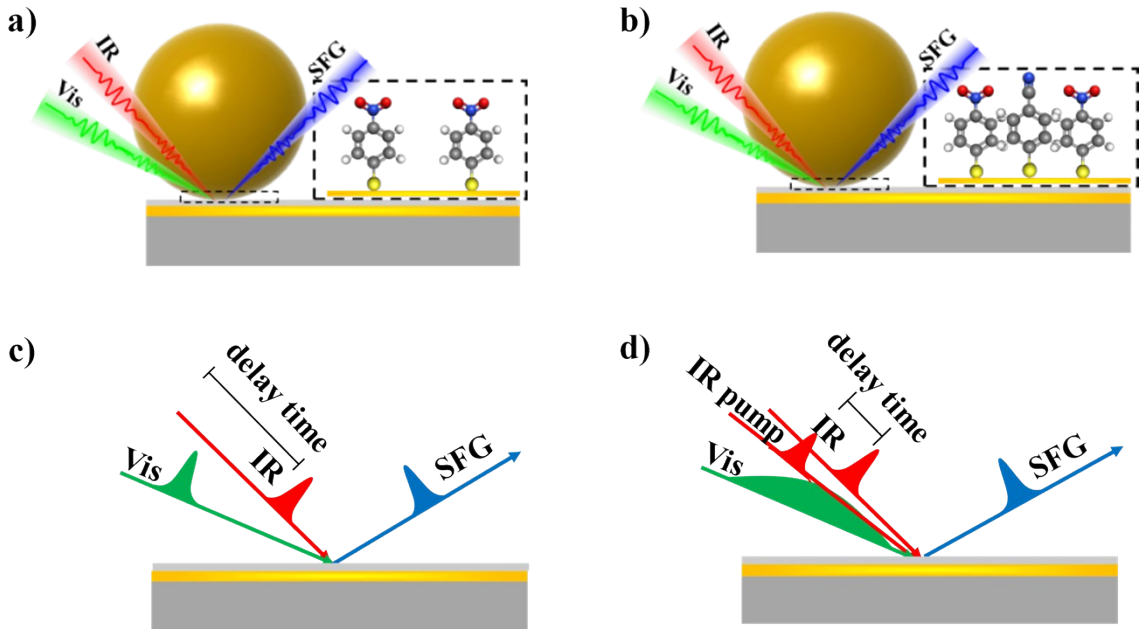

Figure S2. a) A scheme for different concentrations of SAMs; b) A scheme for mixed SAMs; c) A scheme for SFG-FID spectroscopy; d) A scheme for broadband IR-pump SFG-probe spectroscopy.

b) SFG vibrational imaging (SFG-VI)

A schematic diagram of the SFG microscope is shown in Figure S3. It adopts a collinear configuration with a narrowband visible pulse and a broadband mid-infrared pulse. The mid-infrared light is generated by pumping TOPAS with a Ti:sapphire femtosecond laser (centered at 800 nm, bandwidth of 13 nm, 100 fs pulses duration and repetition of 2 kHz, Sepctra Physics, Spitfire Ace seeded by Mai-Tai SP) followed by a non-collinear difference frequency generation system using a $AgGaS_2$ crystal (Chengdu Dien Photoelectric Technology Co., Ltd.). The mid-infrared pulse energy is approximately 7 μJ, which is centered at ~1340 cm^{-1} with a bandwidth of ~200 cm^{-1}. The narrowband

visible light with a bandwidth of about 5 cm^{-1} is generated through a home-built 4-f pulse shaper and optimized by passing through a spatial filter. The collinearity of the visible and infrared pulses is achieved using a dichroic mirror (ISP Optics) that transmits the visible pulse and reflects the infrared pulse. The combined beam is focused onto the sample using a reflective objective (Newport, 15×/0.4 NA). The reflected lights are then separated by a long-pass filter, which isolates the visible pulse and SFG signal. The SFG signal was recorded by a monochromator and CCD, while the visible pulse is used by an imaging system to monitor whether the sample is at the focal point. The sample is placed on a two-axis piezoelectric stage (Coremorrow, P18.XY200S) that allows movement within a 200x200 μm area. All instruments are controlled by home-built LabVIEW software.

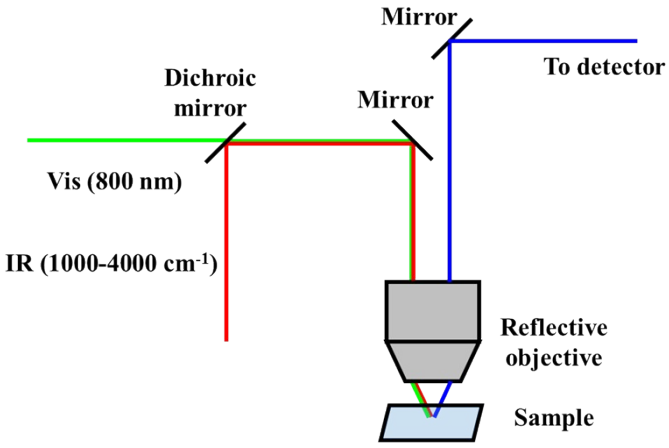

Figure S3. Schematic of SFG-VI.

1.3 Fitting of the SFG-VS signal

The SFG signals were fitted using a standard procedure described in eq. S1.[8]

$$I_{SFG} = B_0 + \left| \chi^{(2)}_{NR} + \sum_{\nu} \frac{A_\nu}{\omega - \omega_\nu + i\Gamma_\nu} \right|^2 \quad \text{(S1)}$$

where B_0 represents the contributing part of the non-SFG process, which may usually come from the background light. $\chi^{(2)}_{NR}$ is the nonresonant background, and A_v, ω_v, and Γ_v are the strength, resonant frequency, and damping coefficient of the vibrational mode (ν), respectively. The peak frequency and bandwidth are used below as ω and Γ, respectively. The effective peak strength $\chi^{(2)}_v$ is defined as A_v/Γ_v. All the fitting parameters can be extracted by fitting the spectra.

1.4 Data analysis of SFG-FID spectra

The data analysis of SFG-FID spectra has been shown in the literatures.[6, 9-11] In FID experiments, the Vis-SFG spectrum can be fitted by eq. S2, which contains a sum of convolutions (conv) of a Gaussian and a Lorentzian for each resonant feature to account for the inhomogeneous broadening.

$$I_{SFG}(\omega) \propto \left| \sum_v conv\{ \frac{A_v}{\omega - \omega_v + i\left(\Gamma_v + \frac{\Delta\omega_{Vis}}{2}\right)} \times \exp\left(-\left(-\frac{\omega - \omega_v}{\Gamma_{inh,\ v}}\right)^2 \right) \} + \frac{|A_{NR}|}{\Delta\omega_{IR}} e^{i\varepsilon} \right|^2 exp \left\{ -\left(\frac{\omega - \omega_0}{\Delta\omega_{IR}}\right)^2 \right\} \tag{S2}$$

where ω_0 and $\Delta\omega_{IR}$ are the center frequency and width of the IR pulse, respectively.

The relationship between the time-domain SFG signal intensity and the delay (τ) between the incident IR pulse and the visible pulse is expressed by eqs. S3-S5:

$$I_{SFG}(\tau) \propto \int_{-\infty}^{\infty} dt \left| P^{(2)}(t,\tau) \right|^2 \tag{S3}$$

$$P^{(2)}(t,\tau) \propto E_{Vis}(t-\tau)P^{(1)}(t) \quad \text{(S4)}$$

$$P^{(1)}(t) = \int_{-\infty}^{\infty} dt' E_{IR}(t-t')S(t') \quad \text{(S5)}$$

$$S(t) = \left[\delta(t)|A_{NR}|\exp(i\varepsilon) - i\theta(t)\sum_{\nu} A_{R,\nu} exp(2\pi c(-i\omega_{\nu}t - \Gamma_{\nu}t))\right] + c.c. \quad \text{(S6)}$$

where the second-order polarization $P^{(2)}$ at a given time delay, τ, expressed in eq. S4, is created by mixing the first-order polarization $P^{(1)}$ induced by the IR excitation (E_{IR}) and the polarization induced by the Vis upconverting field (E_{Vis}), as expressed in eq. S5. To simplify the analysis, we ignore the contribution of inhomogeneous broadening. eq. S6 describes the response of the system, *S(t)*, where *δ(t)* is the delta function, *θ(t)* is the Heaviside step function, and *c* is the speed of light. $1/[2\pi c\Gamma_{\nu}]$ represents the total dephasing time ($T_{2,\nu}$) of the vibration mode ν.

2. Static ppp SFG spectra at 1100-1800 cm^{-1} for different concentrations of NPoM-SAMs

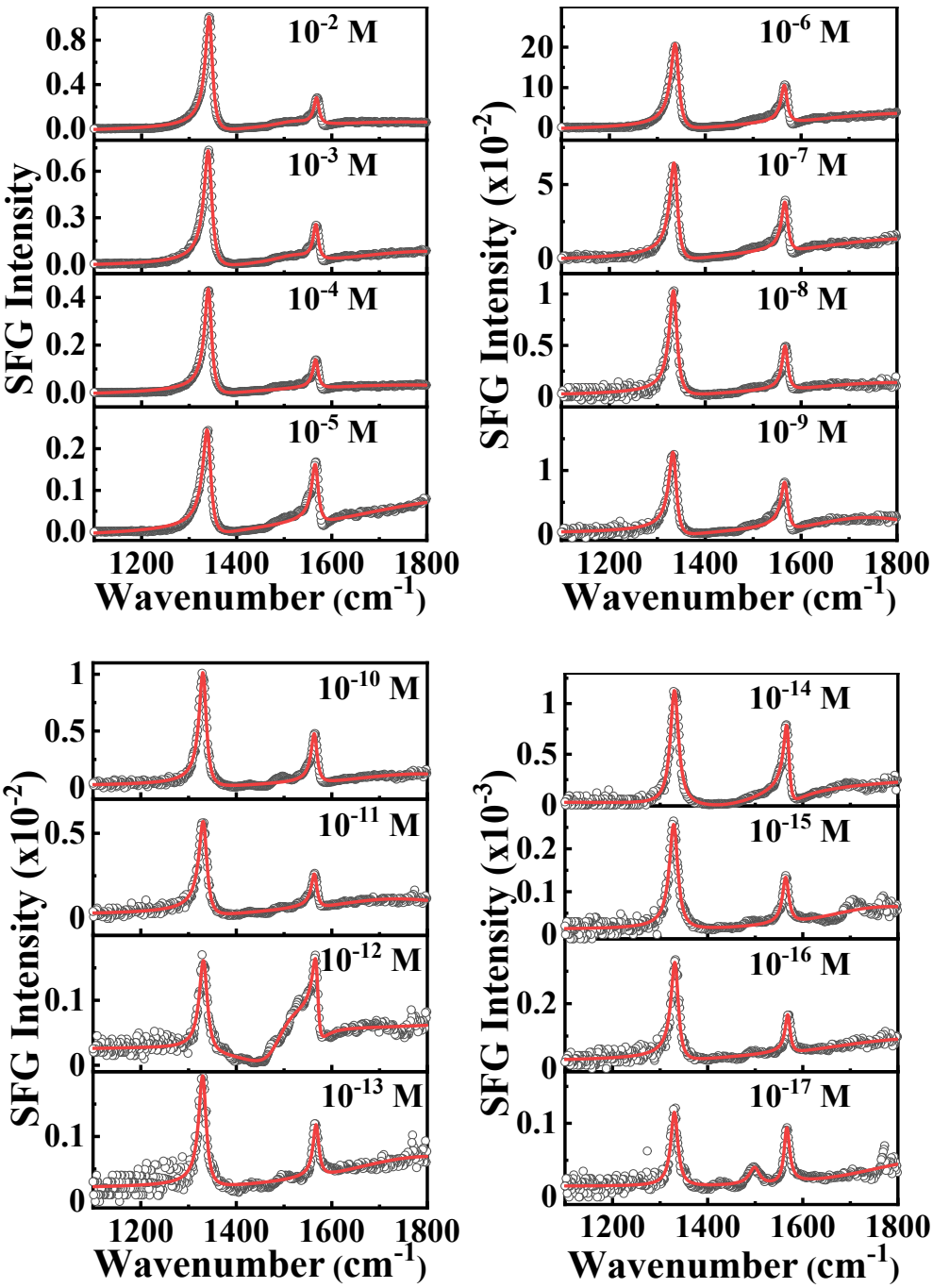
SFG Intensity
SFG Intensity (x10-2)
SFG Intensity (x10-3)
Wavenumber (cm-1)
10-2 M
10-3 M
10-4 M
10-5 M
10-6 M
10-7 M
10-8 M
10-9 M
10-10 M
10-11 M
10-12 M
10-13 M
10-14 M
10-15 M
10-16 M
10-17 M

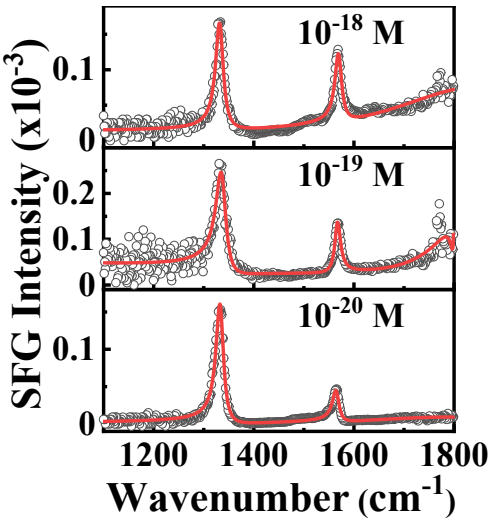

Figure S4. Static ppp SFG spectra of NPoM-SAMs at 1100-1800 cm^{-1} for *C*=10^{-2}, 10^{-3}, 10^{-4}, 10^{-5}, 10^{-6}, 10^{-7}, 10^{-8}, 10^{-9}, 10^{-10}, 10^{-11}, 10^{-12}, 10^{-13}, 10^{-14}, 10^{-15}, 10^{-16}, 10^{-17}, 10^{-18}, 10^{-19} and 10^{-20} M. The symbol "*C*" represents the concentration of the solution that was used to prepare the SAMs.

Table S1. Fitting parameters for the ppp spectra shown in Figure S4.

ppp		**10^{-2}**	**10^{-3}**	**10^{-4}**	**10^{-5}**
	B_0	-0.04	-0.02	-0.03	-0.02
	$\chi_{NR}^{(2)}$	-0.02	-0.02	-0.01	0.01
	A	8.6	7.7	2.5	1.8
Peak 1	ω (cm^{-1})	1345.0	1343.3	1341.0	1339.7
	Γ (cm^{-1})	9.2	10.0	8.2	10.3
	A	2.2	2.2	1.7	0.8
Peak 2	ω (cm^{-1})	1570.1	1570	1567.6	1568.1
	Γ (cm^{-1})	6.5	6.2	6.7	6.3
	A	2.6			
Peak 3	ω (cm^{-1})	1524.5			
	Γ (cm^{-1})	43.1			

ppp		**10^{-6}**	**10^{-7}**	**10^{-8}**	**10^{-9}**

	B_0	-0.01	0	0	0
	$\chi_{NR}^{(2)}$	-0.002	0	0.01	-0.001
	A	3.9	2.1	1.9	1.0
Peak 1	ω (cm^{-1})	1338.4	1336.3	1335.4	1334.2
	Γ (cm^{-1})	10.3	9.8	9.7	9.6
	A	1.5	0.9	0.6	0.5
Peak 2	ω (cm^{-1})	1567.5	1569	1566.5	1567.2
	Γ (cm^{-1})	7.8	8.0	8.3	8.5

ppp		**10^{-10}**	**10^{-11}**	**10^{-12}**	**10^{-13}**
	B_0	0	0	0	0
	$\chi_{NR}^{(2)}$	0	0	0	0
	A	0.9	0.7	0.3	0.3
Peak 1	ω (cm^{-1})	1332.9	1333.6	1333.7	1332.1
	Γ (cm^{-1})	9.2	10.2	10.2	9.6
	A	0.4	0.2	0.1	0.1
Peak 2	ω (cm^{-1})	1565.9	1566.2	1570.6	1569.3
	Γ (cm^{-1})	7.6	7.1	7.0	7.4
	A			-0.2	
Peak 3	ω (cm^{-1})			1487.4	
	Γ (cm^{-1})			49.8	

ppp		**10^{-14}**	**10^{-15}**	**10^{-16}**	**10^{-17}**
	B_0	0	0	0	0
	$\chi_{NR}^{(2)}$	0	0	0	0
	A	0.3	0.2	0.1	0.08
Peak 1	ω (cm^{-1})	1332.0	1331.1	1332.2	1332.1
	Γ (cm^{-1})	10.6	10.9	9.4	9.0
	A	0.1	0.06	0.04	0.04
Peak 2	ω (cm^{-1})	1570.0	1566.3	1571.0	1568.0
	Γ (cm^{-1})	7.1	8.1	6.4	7.1
	A				0.04

ω (cm^{-1})		1501.3
Γ (cm^{-1})		13.1

ppp		**10^{-18}**	**10^{-19}**	**10^{-20}**
	B_0	0	0	0
	$\chi_{NR}^{(2)}$	0	0	0
	A	0.1	0.1	0.1
Peak 1	ω (cm^{-1})	1332.2	1332.2	1333.1
	Γ (cm^{-1})	9.4	9.7	9.1
	A	0.05	0.06	0.04
Peak 2	ω (cm^{-1})	1571.3	1570.2	1566.7
	Γ (cm^{-1})	8.1	7.2	7.8

Note: The symbol "*C*" represents the concentration of the solution that was used to prepare the SAMs.

3. Images constructed with the ν_{NO2} SFG peak area.

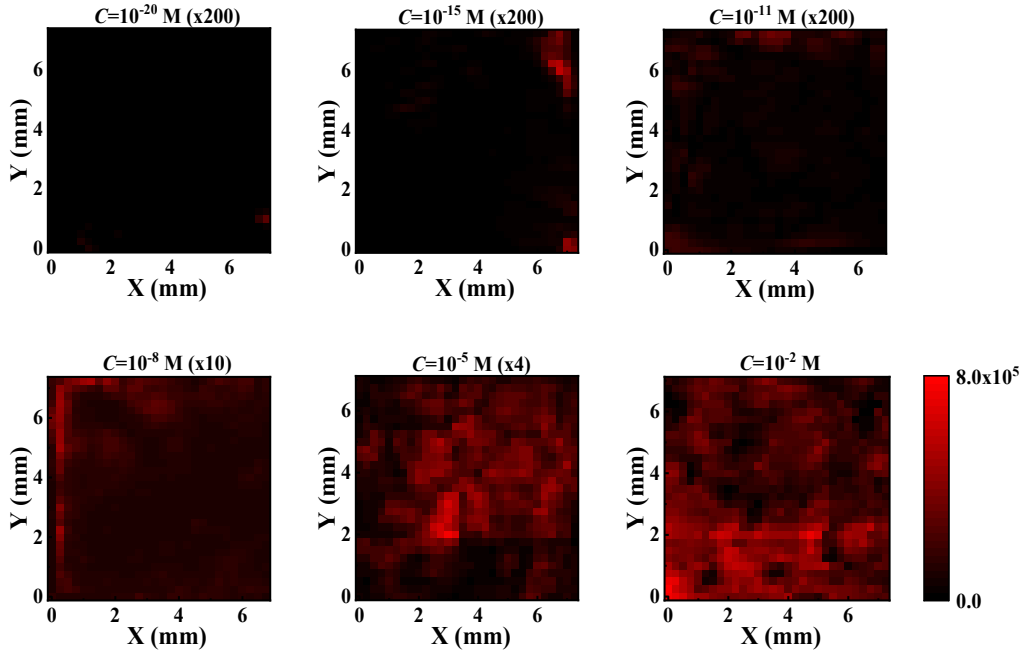

Figure S5. Images constructed with the ν_{NO2} SFG peak area of samples prepared with *C*=10^{-20} M, *C*=10^{-15} M, *C*=10^{-11} M, *C*=10^{-8} M, *C*=10^{-5} M, and *C*=10^{-2} M.

It should be noted that the full-range sample imaging demonstrated in Figure S5 is not achieved using the high-precision co-linear imaging tool demonstrated in S1.2b) but rather the SFG-VS (S1.2a)) combined with the two-axis piezoelectric stage. The signals from molecules within the nanocavity are influenced by many factors, such as the number of molecules and the intensity of the hotspots. The signal intensity varies significantly across the entire surface, as shown in Figure S5.

4. Static ppp SFG spectra in the NO_2 stretching region for different concentrations of Au-SAMs

Due to the weak signal on the Au film, Au-SAMs show negative resonance signals when the concentration is low. In contrast, the resonance signals in the NPoM-SAMs samples are all positive due to the strong enhancement effect produced by the nanocavity and the small non-resonant signals of the Au NPs.

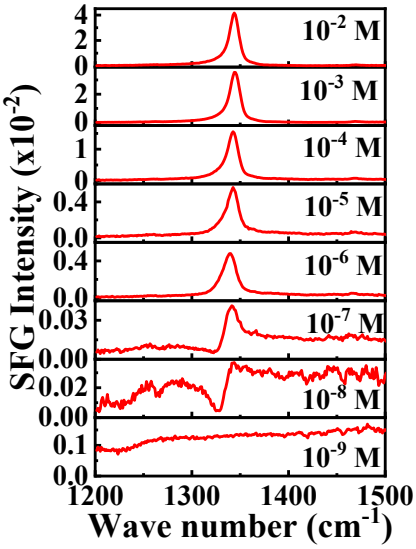

Figure S6. Static ppp SFG spectra of Au-SAMs in the NO_2 stretching region for C=10^{-2},

10^{-3}, 10^{-4}, 10^{-5}, 10^{-6}, 10^{-7},10^{-8} and 10^{-9} M. The symbol "*C*" represents the concentration of the solution that was used to prepare the SAMs.

Table S2. Fitting parameters for the ppp spectra shown in Figure S6.

ppp		**10^{-2}**	**10^{-3}**	**10^{-4}**	**10^{-5}**
	B_0	2E-4	E-5	5E-5	3E-5
	$\chi_{NR}^{(2)}$	-0.01	-0.01	-0.007	0
	A	1.2	1.2	0.8	0.5
Peak 1	ω (cm^{-1})	1345.1	1344.7	1342.7	1341.7
	Γ (cm^{-1})	5.9	6.1	6.7	7.6

ppp		**10^{-6}**	**10^{-7}**	**10^{-8}**	**10^{-9}**
	B_0	3E-5	2E-5	2E-5	-
	$\chi_{NR}^{(2)}$	0	0.01	-0.05	-
	A	0.5	0.1	-0.05	-
Peak 1	ω (cm^{-1})	1339.0	1335.9	1334.0	-
	Γ (cm^{-1})	8.0	8.1	6.0	-

5. The effect of surface roughness

In this study, the gold film was fabricated by using Sputter-Lesker-PVD75 (USTC Center for Micro- and Nanoscale Research and Fabrication). The gold film used in our study has an in-plane non-uniformity of approximately 1% and a high surface smoothness (Figure S7). It is evident that the reproducibility of the samples prepared from different batches of gold films in our experiments was very good.

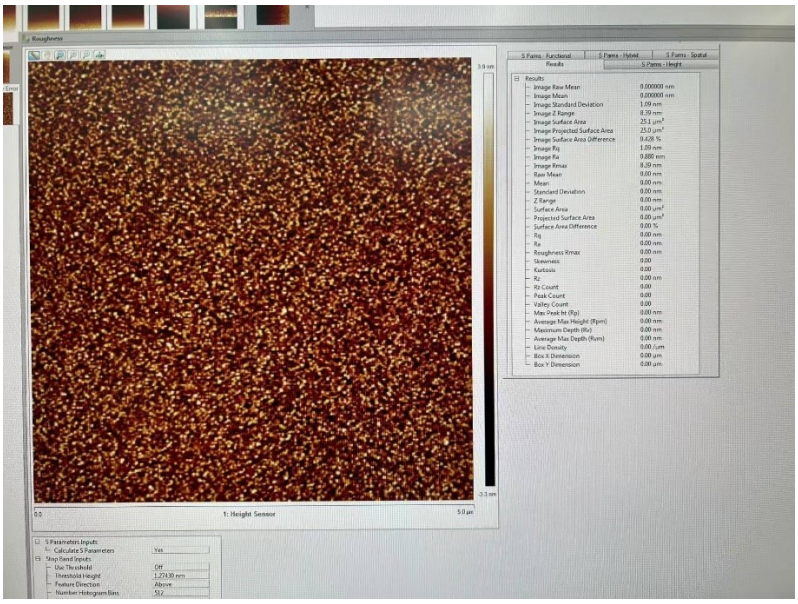

Figure S7. The roughness of Au films.

Although the Au film may have terraces and step features, their effect on the SFG intensity is much smaller than the effect of nanocavity on the signal enhancement (Figure S8). Figure S8 shows the SFG images constructed with the ν_{NO2} SFG peak area of NPoM-SAM and Au-SAM. In Figure S8, the signal of Au-SAM is relatively homogeneous, while the signal of NPoM-SAM is more affected by hotspots and is not uniform. In addition, the signal of NPoM-SAM is much stronger than that of Au-SAM.

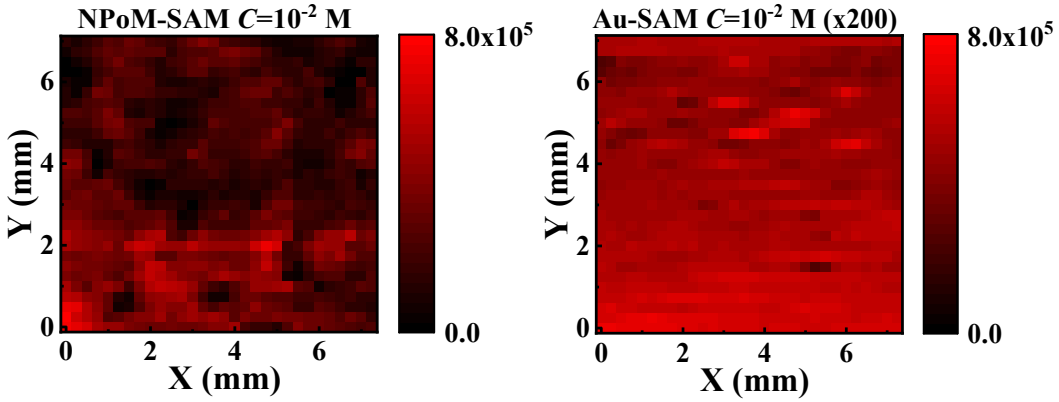

Figure S8. Images constructed with the ν_{NO2} SFG peak area of NPoM-SAM and

Au-SAM.

6. SFG-FID spectra for typical concentrations of NPoM-SAMs

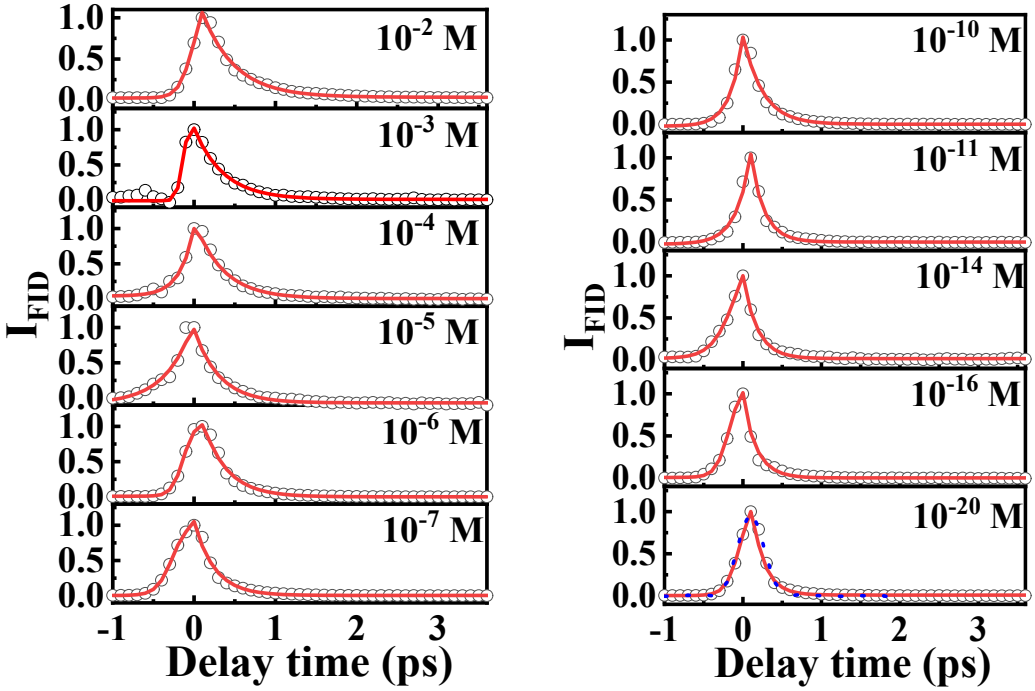

Figure S9. SFG-FID spectra, where the blue dashed line is the cross-correlation trace between the visible and IR regions. 10^{-2}, 10^{-3}, 10^{-4}, 10^{-5}, 10^{-6}, 10^{-7}, 10^{-10}, 10^{-11}, 10^{-14}, and 10^{-20} M represent the concentration of the solution that was used to prepare the SAMs.

Figure S9 shows the SFG-FID spectra of ν_{NO2} at several typical concentrations, and when the concentration is very low, the dephasing process is very close to the cross-correlation trace, indicating that the dephasing process is very fast when the concentration is low.

7. The ppp $\chi^{(2)}$ decay of ν_{NO2} for typical concentrations of NPoM-SAMs

When performing dynamics experiments, the exposure time needs to be adjusted to achieve good signal-to-noise. The exposure time is 5 s for high concentration samples while the exposure time is 300 s for low concentration samples. The final spectral intensity was normalized by the exposure time.

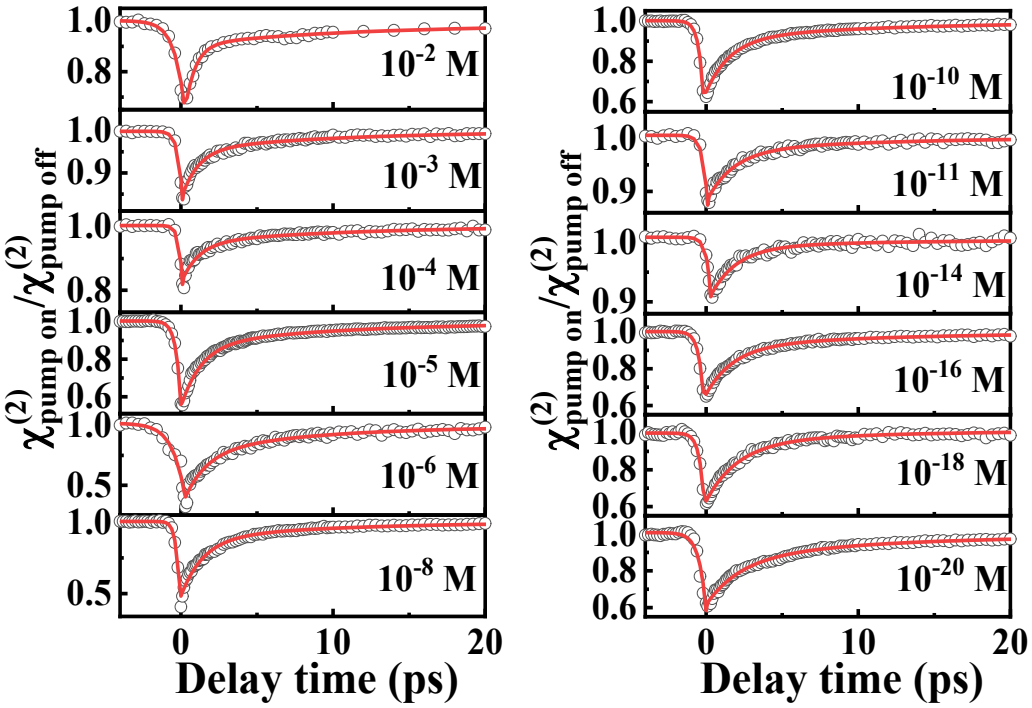

Figure S10. The ppp $\chi^{(2)}$ decay of v_{NO2} for typical concentrations of NPoM-SAMs. 10^{-2}, 10^{-3}, 10^{-4}, 10^{-5}, 10^{-6}, 10^{-8}, 10^{-10}, 10^{-11}, 10^{-14}, 10^{-16}, 10^{-18}, and 10^{-20} M represent the concentration of the solution that was used to prepare the SAMs.

Table S3. Relaxation times for different *C*.

C	A_1	T_1 (ps)	A_2	T_2 (ps)
10^{-2}	-0.21 (±0.01)	0.7 (±0.1)	-0.07 (±0.01)	9.6 (±1.4)
10^{-3}	-0.10 (±0.01)	1.1 (±0.1)	-0.04 (±0.01)	10.0 (±0.9)

10^{-4}	-0.11 (±0.01)	1.1 (±0.1)	-0.05 (±0.01)	11.4 (±1.4)
10^{-5}	-0.30 (±0.01)	1.3 (±0.1)	-0.12 (±0.01)	9.6 (±0.5)
10^{-6}	-0.36 (±0.03)	1.4 (±0.2)	-0.23 (±0.03)	8.0 (±1.0)
10^{-8}	-0.40 (±0.01)	1.5 (±0.1)	-0.12 (±0.01)	10.0 (±0.5)
10^{-10}	-0.26 (±0.01)	1.6 (±0.1)	-0.08 (±0.01)	11.4 (±0.8)
10^{-11}	-0.08 (±0.01)	1.7 (±0.1)	-0.03 (±0.01)	10.9 (±2.0)
10^{-14}	-0.08 (±0.01)	1.7 (±0.3)	-0.01 (±0.007)	10.1 (±1.5)
10^{-16}	-0.25 (±0.01)	1.8 (±0.1)	-0.08 (±0.01)	11.1 (±1.0)
10^{-18}	-0.31 (±0.02)	2.1 (±0.2)	-0.07 (±0.02)	10.0 (±2.5)
10^{-20}	-0.23 (±0.02)	2.2 (±0.1)	-0.14 (±0.01)	10.1 (±1.0)

Note: The symbol "*C*" represents the concentration of the solution that was used to prepare the SAMs.

8. Static ppp SFG spectra at 1250-1700 cm^{-1} for different R_{NTP}

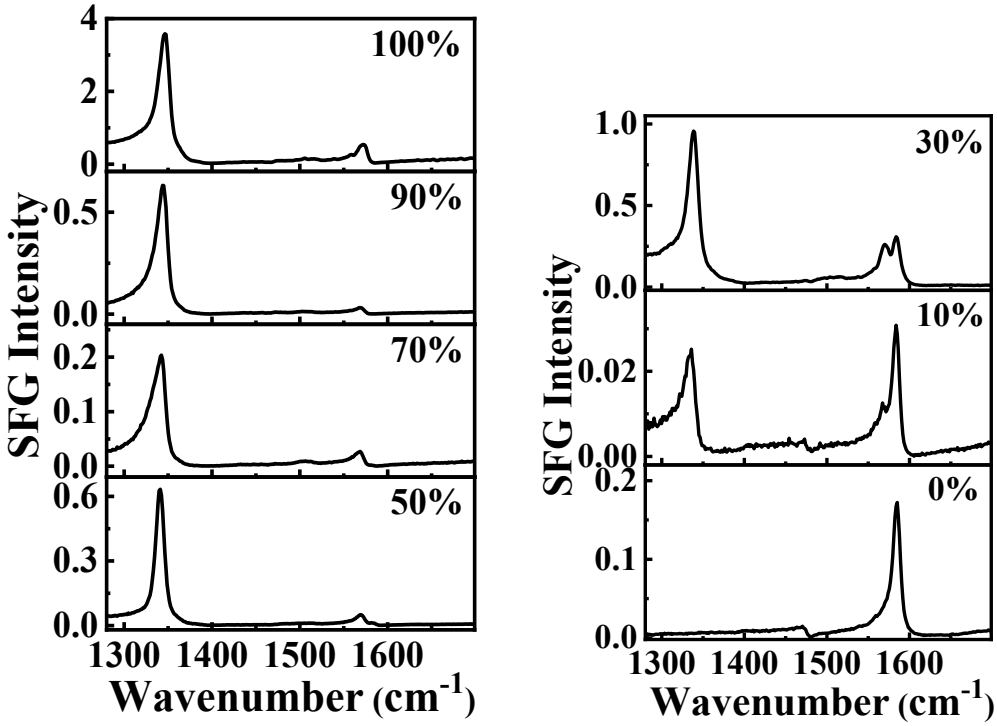

Figure S11. Static ppp SFG spectra at 1250-1700 cm^{-1} for R_{NTP}=100%, 90%, 70%, 50%, 30%, 10%, and 0%.

The non-monotonic variation of the signal strength arises from the difference in the local enhancement effect, which is common in the nanocavity system. Although the signal intensity varies in different regions of the sample, the intrinsic information such as peak frequency and vibrational relaxation lifetime remain consistent. In addition, due to the fact that several experiments were done, Figure 4 and Figure S11 do not present the same set of data, so there will be a difference in the values. As shown in Figure S11, when R_{NTP}=0, there is no information on the resonance peaks of ν_{NO2}. Therefore, the case of R_{NTP} =0 was not considered in the following SFG-FID and vibrational relaxation dynamics analyses.

Table S4. Fitting parameters for the ppp spectra shown in Figure S11.

ppp		**100%**	**90%**	**70%**	**50%**
	B_0	0	0	-0.02	0
	$\chi_{NR}^{(2)}$	-0.44	-0.16	-0.14	-0.07
	A	15.1	6.0	3.1	4.3
Peak 1	ω (cm^{-1})	1346.2	1343.2	1340.6	1339.2
	Γ (cm^{-1})	8.5	7.9	9.3	5.6
	A	2.4	0.6	0.3	1.4
Peak 2	ω (cm^{-1})	1572.1	1571.3	1568.0	1568.2
	Γ (cm^{-1})	4.2	6.4	5.0	6.9
	A				-0.1
Peak 3	ω (cm^{-1})				1580
	Γ (cm^{-1})				6.0

ppp		**30%**	**10%**	**0%**
	B_0	0.02	0	0
	$\chi_{NR}^{(2)}$	-0.16	-0.05	-0.04
	A	5.6	0.9	0.4
Peak 1	ω (cm^{-1})	1337.0	1335.0	1468.9
	Γ (cm^{-1})	7.3	7.8	5.2
	A	2.0	0.1	2.3
Peak 2	ω (cm^{-1})	1569.4	1568.0	1582.8
	Γ (cm^{-1})	6.5	5.0	5.8
	A	2.8	0.8	
Peak 3	ω (cm^{-1})	1581.8	1582.9	
	Γ (cm^{-1})	6.1	5.1	

9. Relaxation times of Figure 4c

Table S5. Relaxation times for different R_{NTP}.

R_{NTP}	A_1	T_1 (ps)	A_2	T_2 (ps)
100%	-0.24 (±0.01)	0.7 (±0.1)	-0.11 (±0.01)	9.7 (±0.6)

90%	-0.10 (±0.01)	0.9 (±0.1)	-0.03 (±0.01)	10.1 (±0.9)
70%	-0.12 (±0.02)	1.1 (±0.1)	-0.06 (±0.01)	10.8 (±0.8)
50%	-0.15 (±0.01)	1.5 (±0.1)	-0.08 (±0.03)	9.7 (±0.7)
30%	-0.19 (±0.01)	1.8 (±0.1)	-0.11 (±0.04)	10.0 (±0.4)
10%	-0.34 (±0.02)	2.1 (±0.2)	-0.11 (±0.02)	10.3 (±1.6)

10. Typical SFG spectra for NPoM-SFG-VI

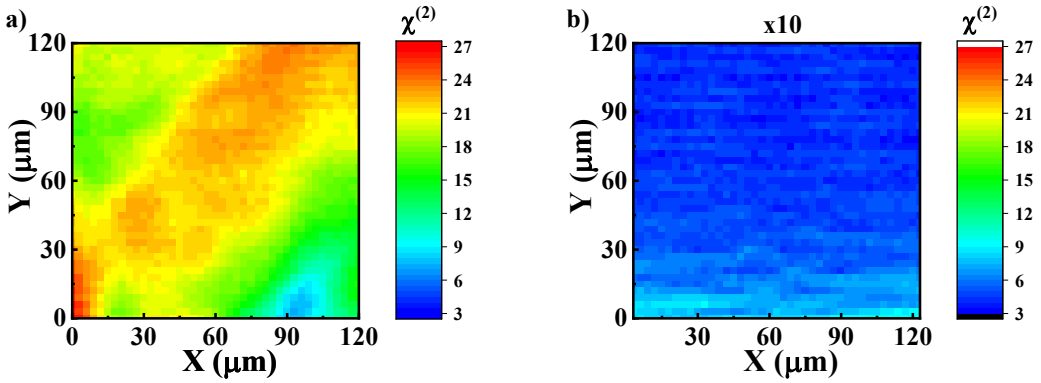

Figure S12. The imaging constructed with the microzone peak strength ($\chi^{(2)}$) of ν_{NO2}: a) the sample prepared with C=10^{-2} M; b) the sample prepared with C=10^{-8} M. The symbol "*C*" represents the concentration of the solution that was used to prepare the SAMs.

It is worth mentioning that the SFG intensity at different microregions depends on the hotspot strength and there is no correlation between the local microzone concentration and the SFG intensity. Additionally, the SFG-VI experiment has relatively harsh requirements on the signal strength of the samples, and the presence of resonance signals in the ordinary SFG-VS experiment does not ensure that the SFG-VI experiment can be carried out. However, the signal is effectively enhanced by the NPoMs, which allows the imaging of

samples even at such a low concentration of 10^{-8} M (Figure S12b). It is difficult to perform SFG-VI experiments on samples with lower concentrations, which are limited by signal strength and randomness of occurrence. In summary, the NPoM-SFG-VI technique has demonstrated the superiority of high sensitivity and spatial resolution for the resolution of interfacial microregion information, and we look forward to the development of means for direct single-molecule visualization in the future.

REFERENCES

(1) J. F. Li, X. D. Tian, S. B. Li, J. R. Anema, Z. L. Yang, Y. Ding, Y. F. Wu, Y. M. Zeng, Q. Z. Chen, B. Ren, Z. L. Wang and Z. Q. Tian, Surface Analysis Using Shell-Isolated Nanoparticle-Enhanced Raman Spectroscopy, *Nat. Protoc.,* 2013, **8**, 52-65.

(2) H. Y. Jung, Y. K. Park, S. Park and S. K. Kim, Surface Enhanced Raman Scattering from Layered Assemblies of Close-Packed Gold Nanoparticles, *Anal. Chim. Acta,* 2007, **602**, 236-243.

(3) Y. K. Park and S. Park, Directing Close-Packing of Midnanosized Gold Nanoparticles at a Water/Hexane Interface, *Chem. Mater.,* 2008, **20**, 2388-2393.

(4) J. J. Tan, B. X. Zhang, Y. Luo and S. J. Ye, Ultrafast Vibrational Dynamics of Membrane-Bound Peptides at the Lipid Bilayer/Water Interface, *Angew. Chem. Int. Ed.*, 2017, **56**, 12977-12981.

(5) J. J. Tan, J. H. Zhang, C. Z. Li, Y. Luo and S. J. Ye, Ultrafast Energy Relaxation

Dynamics of Amide I Vibrations Coupled with Protein-Bound Water Molecules, *Nat. Commun*., 2019, **10**, 1010.

(6) J. H. Zhang, R. Q. Pei, J. J. Tan, Z. J. Ni, S. J. Ye and Y. Luo, Visualizing Water Monomers and Chiral $OH^-(H_2O)$ Complexes Infiltrated in a Macroscopic Hydrophobic Teflon Matrix, *J. Am. Chem. Soc.*, 2023, **145**, 26925-26931.

(7) J. J. Tan, Z. J. Ni and S. J. Ye, Protein-Water Coupling Tunes the Anharmonicity of Amide I Modes in the Interfacial Membrane-Bound Proteins, *J. Chem. Phys.*, 2022, **156**, 105103.

(8) Y. R. Shen, *The Principles of Nonlinear Optics*, Wiley-Interscience, New York, NY, USA, United States, 1984.

(9) A. Eftekhari-Bafrooei, S. Nihonyanagi and E. Borguet, Spectroscopy and Dynamics of the Multiple Free OH Species at an Aqueous/Hydrophobic Interface, *J. Phys. Chem. C*, 2012, **116**, 21734-21741.

(10) A. Boulesbaa and E. Borguet, Vibrational Dynamics of Interfacial Water by Free Induction Decay Sum Frequency Generation (FID-SFG) at the $Al_2O_3(1120)/H_2O$ Interface, *J. Phys. Chem. Lett.*, 2014, **5**, 528-533.

(11) A. Boulesbaa and E. Borguet, Capturing the Ultrafast Vibrational Decoherence of Hydrogen Bonding in Interfacial Water, *J. Phys. Chem. Lett.*, 2016, **7**, 5080-5085.